Research Article | Vol. 11, No. 3 / 1 March 2021 / Optical Materials Express 707

Optical Materials EXPRESS

Argon bubble formation in tantalum oxide-based films for gravitational wave interferometer mirrors

REBECCA B. CUMMINGS,[1,*] RICCARDO BASSIRI,[2] IAIN W. MARTIN,[1] AND IAN MACLAREN[1]

[1]Department of Physics and Astronomy, The University of Glasgow, Glasgow, G12 8QQ, UK
[2]E. L. Ginzton Laboratory, Stanford University, Stanford, California 94305, USA
[*]r.cummings.1@research.gla.ac.uk

Abstract: The argon content of titanium dioxide doped tantalum pentoxide thin films was quantified in a spatially resolved way using high angle annular dark field (HAADF) images and DualEELS (a form of electron energy loss spectroscopy (EELS) that takes two spectra in quick succession from the highs and low-loss region). Films annealed at 300 °C, 400 °C, and 600 °C were investigated to see if there was a relationship between annealing temperature and bubble formation. It was shown using HAADF imaging that argon is present in most of these films and that bubbles of argon start to form after annealing at 400 °C and coarsen after annealing at 600 °C. A semi-empirical standard was created for the quantification using argon data from the EELS Atlas and experimental data scaled using a Hartree Slater cross-section. The density and pressure of argon within the bubbles were calculated for 35 bubbles in the 600 °C sample. The bubbles had a mean diameter, density, and pressure of 22 Å, 870 kg/m^3 and 400 MPa, respectively. The pressure was calculated using the Van der Waals equation. The bubbles may affect the properties of the films, which are used as optical coatings for mirrors in gravitational wave detectors. This spatially resolved quantification technique can be readily applied to other small noble gas bubbles in a range of materials.

1. Introduction

In recent years, gravitational waves from merging binary black holes [1–5] and binary neutron stars [6] have been detected by the Advanced LIGO [7] and Advanced Virgo [8] gravitational wave detectors. These detectors are modified Michelson interferometers that measure changes, induced by gravitational waves, in the relative separation of mirrors located at the end of km-scale perpendicular arms. The interferometer mirrors have highly-reflective multi-layer optical coatings. Thermal noise arising from thermally-induced vibrations in the coatings is a critical sensitivity limit to current detectors at their most sensitive frequencies [7]. Coating thermal noise is related to the mechanical loss, or internal friction, of the coating materials. Reducing the coating loss is essential to enable the construction of more sensitive detectors, which would be able to detect more gravitational waves from a wider range of astrophysical sources. The current high index layer in the LIGO and Virgo mirrors is amorphous Ta_2O_5, doped with TiO_2 [1,8,9], deposited using argon ion beam deposition [10]. Fully understanding the atomic and nano structure of the mirror coatings is the first step in reducing their mechanical loss.

Recent studies have shown that there are voids in the tantala films [11] and also, based on fitting of ellipsometry data and Rutherford backscattering (RBS) measurements, that the films contain argon [12]. Subsequent work on hafnia thin films showed in those samples that argon lies within the bubbles [13] and in tantala films it was shown that bubbles form on annealing [14].

#416038 https://doi.org/10.1364/OME.416038
Journal © 2021 Received 6 Dec 2020; revised 15 Jan 2021; accepted 26 Jan 2021; published 9 Feb 2021

Optical Materials EXPRESS

Little was known, however, on the form of the argon inside the bubbles, or to what extent they are affected by annealing.

Bubbles of noble gas in materials have been well documented over the years, mainly from ion implantation into solid materials. They are of particular interest for materials used in nuclear reactors, where fission products such as alpha particles and heavier nuclei will implant into the walls of the reactor. Once there, the alpha particles capture electrons and become helium nuclei. The heavier nuclei, especially xenon and krypton, will do the same. Noble gases do not interact strongly in a chemical fashion with their surroundings, so their main effect is local strain. If there are multiple noble gas atoms within a diffusion path length of each other the strain field interaction will cause them to cluster together. If there are enough of them they can form nanoscale or larger bubbles in the material [15–17].

Studying nanoscale gas bubbles in materials requires an imaging method with sufficient resolution to determine the number of interior gas atoms. Transmission electron microscopy (TEM) is such one method but scanning transmission electron microscopy (STEM) offers particular advantages. If the gas inside the bubble has a significantly different density to the material surrounding it, then HAADF imaging (only available in STEM) will show Z-contrast [18]. This contrast is an easy way of telling where there are different elements within the sample. STEM also offers analytical techniques like energy dispersive X-ray spectroscopy (EDX) [19] and EELS [20] and there has been significant work in recent years on absolute quantification using both EDX [21,22] and EELS [23,24]. These techniques have been used to study the density, structure and chemistry of the noble gas bubbles [19,25,26]. There are fewer studies on argon bubbles using TEM as argon is less common as a fission product in nuclear reactors but some do exist [20,27].

This paper uses a combination of HAADF imaging and EELS to study argon in the Ta_2O_5-based coatings; quantifying the argon content in a spatially resolved way. This quantification allows calculations of the density and pressure of the argon within the bubbles.

Previous work done at Glasgow showed that absolute quantification using EELS is possible using a technique called DualEELS [28,29] and an experimental standard for the material being quantified. Quantifying gaseous argon meant the latter presented a serious challenge. There is, however, published EELS data for argon gas [30], which will give the correct edge shape for the pressure used in that experiment. Additionally, it is well known that the Hartree-Slater calculations of cross-sections for $L_{2,3}$ edges of lighter elements are reasonably accurate, so long as the measurement is made at a high enough energy above the edge onset [29,31]. The solution, therefore, to the lack of an experimental standard was found by splicing together the absolute cross-section from the Hartree-Slater calculation at a suitably high energy above the edge and the edge shape from the EELS atlas data [30]. This produced a semi-empirical cross-section that could be used to fit real spectrum images (SI) of materials containing argon. Moreover, since it is an absolute cross-section, the fitting coefficients are quantitatively meaningful [24], which means that the number of argon atoms in every pixel of an SI can be counted and allows for the quantitative mapping of argon at sub-nanometre spatial resolution.

2. Methods

2.1. Sample preparation

The samples in this study were part of a series produced at CSIRO using argon ion beam assisted deposition onto fused silica substrates. They are nominally 75% Ta_2O_5 and 25% TiO_2 in stoichiometry, although characterisation using a similar technique to this paper found they were closer to only 10% TiO_2 [32]. Some of the samples were heat treated in air at a range of temperatures (300, 400 and 600 °C) for 24h. These were prepared for transmission electron microscopy observation using a conventional cross-section preparation method as described by Hart [33].

Optical Materials EXPRESS

2.2. Data collection

STEM observation was performed using a JEOL ARM200F operated at 200 kV, and equipped with a Gatan GIF Quantum ER spectrometer. HAADF images were used to select areas of interest and to analyse the physical structure of the sample. EELS spectrum imaging was used to collect data on the composition at high spatial resolution. In all cases, a convergence angle of 29 mrad was used for the probe. In the EELS, a camera length was chosen to give a collection angle into the spectrometer of 36 mrad. Dual range EELS was used, to collect both the low loss and the high loss together using times of 0.000497238 s and 0.0895028 s and energy offsets of 0 eV and 180 eV, and all data was recorded at a dispersion of 0.5 eV/ch.

2.3. Data processing

The EELS datasets were processed using Gatan Digital Micrograph (DM) using similar methods to those described in previous publications [23,34]. The low- and high-loss SI were first aligned by the zero-loss peak of the low-loss image and then any x-rays that caused a spike larger than 10σ above background were removed. The energy range of the low-loss datasets was cropped to 150 eV so only channels containing useful information remained. The SIs were then run through a principal component analysis plug-in [35] in order to separate real signal from random noise. The high- and low-loss spectra were spliced together and Fourier-logarithm deconvolution [36] was performed to yield a single scattering distribution. This is essential to in order to produce model-based fitting with consistent shapes, even if there are thickness variations in the area analysed [24].

A semi-empirical cross-section of the Ar-$L_{2,3}$ edge was constructed from the EELS atlas [30] edge shape, which has a dispersion of 0.3 eV/channel. First, this dataset was re-binned to 0.5 eV/ch to match the experimental data. This was done using a script based on ideas developed in separate work, which is on the correction of dispersion non-linearities in some EELS data [37]. The Hartree-Slater cross-section for the Ar-$L_{2,3}$ edge was calculated for the experimental conditions used in our analysis. This cross-section was then used to scale the experimentally measured argon edge to give a tail of the correct magnitude, to allow for its use in fitting to the experimental data (Fig. 4)a)).

After this, the experimental datasets were fitted using the multiple linear least squares (MLLS) method as implemented by the standard function in DM. This function fits an experimental SI as the sum of two or more standard spectra and requires several datasets as references. The argon edge cross-section was calculated as described above. The tantala-titania glass standard was estimated by finding an area in the spectrum image where there was little or no argon. This process is straightforward as the Ar-$L_{2,3}$ edge has a strong peak at 250 eV, which is above the edge onset for the Ta-$N_{4,5}$ edge (226 eV) [10,32], but below the Ti-$L_{2,3}$ (454 eV). In some cases, two such spectra were recorded if the area scanned contained a significant thickness variation in the sample, in order to remove any thickness effects. As the fit is made using extracted spectra, rather than the images they produce, you cannot account for a gradient in thickness when only using one spectrum. Using two spectra, one thick and one thin, proved to be enough to account for the variation when fitting the data.

Ultimately, there was no effort to determine Ti-Ta stoichiometry, which has been done previously [10,32]. This means that the only standard required to have a quantitative meaning is the argon one.

The MLLS fit (Fig. 3) was restricted to 220-280 eV so as to not include the carbon K-edge at 284 eV, since C contamination on surfaces could vary with position and skew results. The fitting was an iterative process as it was not always clear from the original image where the boundaries of the bubbles were, and areas chosen for selection of components were adjusted until the fit residuals were minimised. This iterative approach is based on the one used by Annand [38].

Optical Materials EXPRESS

The final fit is a reconstruction of the original image made using the spectra provided, i.e. the matrix component and the argon cross-section. As stated above, the fit coefficients are quantitatively related to the number of atoms illuminated by the beam in each pixel of the SI and so can be used to calculate the areal density of the argon atoms in the bubbles:

$$\frac{dI}{dE} = I_0 \sum_{\text{(elements i)}} \sum_{\text{(shells j)}} N_j \frac{d\sigma_{ij}}{dE}, \tag{1}$$

where $\frac{dI}{dE}$ is the intensity per unit energy at a given energy loss, and $\frac{d\sigma_{ij}}{dE}$ is the partial cross-section of an electron in the *j*th shell of the *i*th atom; as detailed and used in [24]. Specifically, in this case

$$N_{Ar} = \frac{I_{Ar}}{I_0 \sigma(\Delta E)}, \tag{2}$$

where I_{Ar} is the spectrum intensity of the argon edge in the energy range, ΔE, used in the fit, I_0 is the intensity of the zero-loss peak in the low-loss data, and N_{Ar} is the number of argon atoms per unit area. The number of atoms in each column represented by a pixel in an image was calculated by multiplying N_{Ar} by the area of the pixel.

As in previous work, the differential cross-section, $\frac{d\sigma_{ij}}{dE}$ is in units of Barns/eV [24]. In order to convert it to a total cross-section, $\sigma(\Delta E)$, this needs to be integrated over the energy range ΔE and multiplied by the channel width.

The bubbles were assumed to be spherical, based on their appearance in the HAADF images. The diameter of each bubble was taken to be the horizontal diameter from the fit coefficient maps. This horizontal value was taken rather than the vertical because of the drift that can occur when the beam rasters across the sample. It has little effect along the line but between the top and the bottom of the bubble it has a much greater effect, potentially over 1 nm.

A border of one pixel either side of the bubble was also included, based on comparison between elemental maps of argon and HAADF images of the same object. This is because the argon content in the outer part of the bubble will appear negligible because of the very short beam path through the bubble. Not including the border, however, will make the bubble too small and give unrealistically high densities of argon, consequently affecting the pressure calculations. The volume was calculated using the standard equation relating diameter and volume in a sphere.

The pressure inside the bubbles was calculated using the Van der Waals equation of state [39]:

$$(P + \frac{an^2}{V^2})(V - nb) = nRT, \tag{3}$$

where P is pressure, V is volume of gas, n is the number of moles, T is temperature, R is the gas constant and a and b are experimentally derived constants unique to each material (1.345 L^2 bar mol $^{-2}$ and 0.03219 L mol $^{-1}$, respectively, for argon [40]). The ideal gas law could not be used as its assumptions do not hold in this case; at such small volumes and high densities the argon atoms cannot be assumed to be non-interacting point particles.

3. Results and discussion

Figure 1 shows HAADF images of thin areas of two samples, heat treated at 400 °C and 600 °C, respectively. In both cases lower-density (i.e. darker) regions are seen, all a few nm in diameter. They are mostly rounded in appearance, suggesting that they are approximately spherical voids or bubbles. They are clearly larger and more prominent in the sample annealed at the highest temperature. Similar features were seen in the sample heat-treated at 300 °C, but the images were very poor due to sample charging. They were smaller and fainter than those in the 400 °C sample. It would have been possible to recoat the 300 °C annealed sample with carbon to prevent

Optical Materials EXPRESS

the charging but as the bubbles in the 400 °C annealed sample were already difficult to analyse it was not deemed necessary. It was not possible to unambiguously resolve any such features in the non-annealed sample. It can be seen in Fig. 2, however, that argon was still definitely present in these samples. The as deposited sample has a weak edge visible around 250 eV and the edge for the 400 °C annealed sample is as strong as the one in the 600 °C annealed sample.

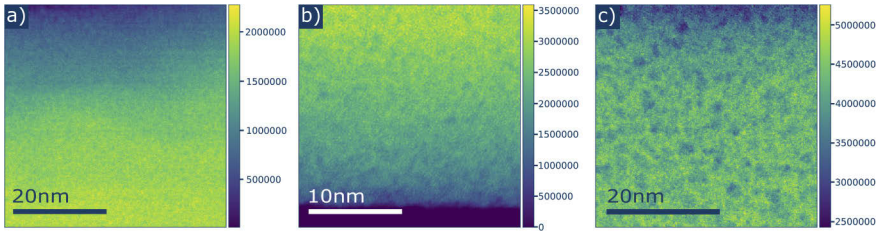

Fig. 1. HAADF images of larger areas containing bubbles: a) the as-deposited sample showing no bubbles; b) the sample annealed at 400 °C for 24 hours, showing small bubbles, the strong contrast variation is due to this image being taken at the very edge of the sample; c) the sample annealed at 600 °C for 24 hours showing larger bubbles, with only a slight thickness increase from top to bottom. In both samples, most bubbles appear rounded, and it is clear there is some range in the bubble sizes in both cases. The colour map is *viridis* from *matplotlib* [41], with the argon bubbles showing up as darker areas. The scale bars show the relative intensities of each image.

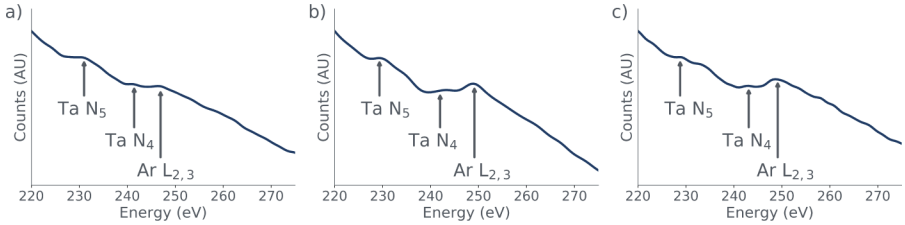

Fig. 2. EELS spectra from three samples all annealed at different temperatures, showing clear evidence that argon is incorporated in all three. The relative intensities of the element edges are proportional to the amount of the element in the material. The tantalum N_5 (226 eV onset) and N_4 (238 eV onset) edges and the argon $L_{2,3}$ edge (248 eV onset) are visible in all of the samples; a) the as-deposited sample; b) 400 °C annealed sample; c) the 600 °C annealed sample.

While the exact sizes of the bubbles are hard to define from the unprocessed datasets it does appear that the average size of the bubbles grows with annealing temperature. Due to the poor signal-to-noise ratio in the 400 °C annealed datasets the full processing procedure was not possible. This means that the size distribution of the bubble diameter comes from the deconvolved-sliced images of the 600 °C annealed datasets only; as there were not enough clearly defined bubbles in the 400 °C annealed datasets to give a reliable distribution of bubble diameter. All data mentioned past this point stem from the 600 °C annealed sample.

The dataset of the MLLS fit shown in Fig. 3 had a thickness gradient in the matrix, which is why there are two matrix components; a thick coefficient and a thin one. It seems the matrix was thicker at the top of the area scanned (as shown in Fig. 3). Not all samples displayed this gradient.

As stated, the fitting was an iterative process. Figure 4 shows the contributions to the overall spectrum from a bubble inside each of the three different components: the background-subtracted argon cross-section (a), and the thin and thick matrix standard spectra (b). These spectra make it

Optical Materials EXPRESS

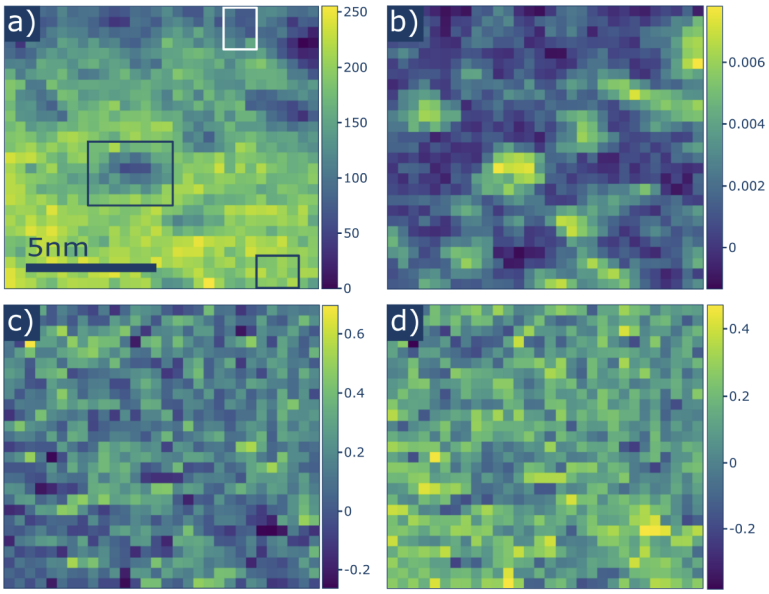

Fig. 3. MLLS fit component maps for one of the datasets annealed at 600 °C; a) the fit to the single scattering distribution, with annotations to show where the matrix component spectra were taken from; top = thick matrix, bottom = thin matrix. The middle rectangle denotes an example of how the edges of the bubbles were drawn, with a border round the area of brightest intensity; b) the argon coefficient map, showing areas of intensities where the bubbles lie; c) thick matrix coefficient; d) thin matrix coefficient.

clear that even with an obvious bubble, the argon signal itself is a tiny fraction of the total EELS signal in this energy range. It is only through the intrinsic noise-reducing properties of the MLLS fit (which fits through the random noise) that such weak features could be reliably extracted and quantified. These spectra were calculated by multiplying the fit coefficient for the area by the standard spectrum.

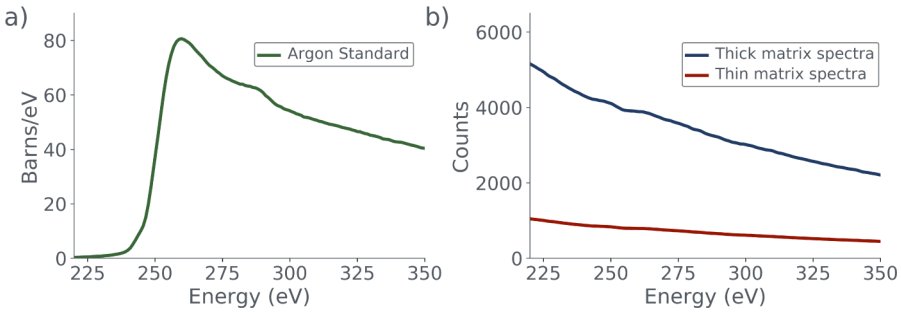

Fig. 4. The contributions of the components of the MLLS fit for one bubble (i.e. the standard spectrum multiplied by the fit coefficient); a) for argon, based on the background-subtracted cross-section; b) for thin and thick matrix components. Note the difference in the magnitude of the y-axes scale, the matrix components dominate, even in a bubble area, and the signal from the argon in the bubble is always a tiny fraction of the total EELS signal.

Figure 3 shows the actual maps of the fit coefficients for the three components shown in Fig. 4. The fit coefficient for the argon is of particular interest, as this can be directly interpreted into an

Optical Materials EXPRESS

absolute number of argon atoms per column (Eqs. (1 and (2)). From this the argon density inside of the bubbles can be calculated, as well as the pressure Eq. (3).

The matrix coefficients were made using spectra extracted from the single scattering distribution rather than a standard, so it is not possible to determine the absolute number of atoms from them.

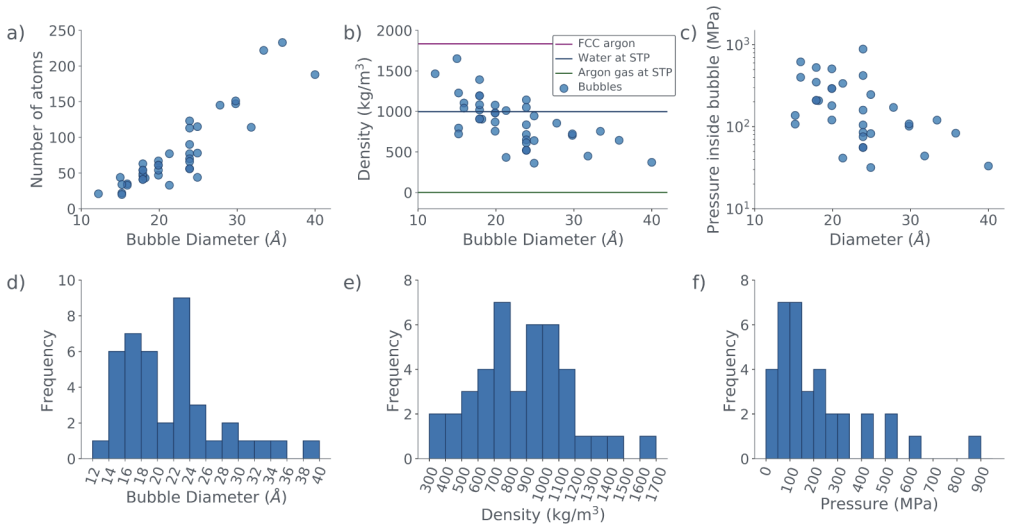

Fig. 5. Analysis of the argon bubbles in the 600 °C sample; a) number of argon atoms in bubble against their diameter; b) density of the argon bubbles, with lines representing the density of argon gas at standard pressure and temperature (STP), water and argon arranged in the tightest possible face-centered cubic (FCC) packing [40]; c) pressures of the bubbles against their diameter; d) distribution of bubble diameters; e) distribution of bubble densities; f) distribution of bubble pressures.

Figure 5 shows that the number of atoms per bubble increases with bubble diameter, as might be expected. The precision with which the diameter can be measured is limited by pixel size (3-6 Å) and it is one potential cause of the wide range in the number of argon atoms in bubbles of the same size. It is hard to tell from the limited number of samples what the precise nature of the relationship between number of atoms and diameter is (linear, quadratic, cubic etc). The bubbles that were especially numerically dense are most likely two bubbles laid over each other. The diameters measured are in good agreement with those taken from HAADF images in previous studies [14].

For all of the bubbles that made up the final pressure analysis, the number of atoms per bubble is below the number that could fit assuming the argon was in crystal form (i.e. the maximum number of argon atoms that could physically fit in the bubble, ignoring temperature). FCC argon has a lattice parameter of 5.45 Å at 81 K, which translates to an atom spacing of 3.85 Å. The data suggests most of the bubbles are still in gas form but some of the smallest may be a high density fluid. Previous work on xenon and krypton suggests it can be solid at room temperature in bubbles formed from ion implantation [42–44]. There is some evidence that argon can also form solid bubbles, with a lattice parameter around 5.15 Å [44–46].

The bubbles are far less dense than the Ta_2O_5 surrounding them, which has a density of ~7750 kg/m^3 [32]. This explains the HAADF contrast of Fig. 1, where the bubbles are darker than the surrounding Ta_2O_5 matrix.

Using RBS, a similar sample was found to contain 3% argon [12]. Comparing the number of atoms in the bubbles with the total number of atoms in the matrix (calculated using the number densities of atoms and mean free paths for inelastic scattering in Ta_2O_5 and TiO_2 [32,47]), results

Optical Materials EXPRESS

in a much lower argon contribution (<1%). The remaining argon is likely still in the matrix as individual interstitial atoms or sub-nanometre clusters and not the bubbles, although it might continue to precipitate out into bubbles if a longer heat treatment were applied. Argon near the surface of these samples may also have been lost due to damage during sample preparation. A bubble volume fraction calculation was not done as it would require an argon-free Ta_2O_5 film with which to compare the argon-containing samples. Preliminary calculations suggest, however, that it may be around 4-5%, on account of the relatively low density of the bubbles, when compared with the Ta_2O_5.

As the density of the argon inside the bubbles is well above the density of argon at STP [40], the ideal gas law will not provide an accurate description of the pressure inside of the bubbles. The Van der Waals equation of state should describe the situation better at higher densities, and this put the average pressure inside of the bubbles on the order of 100 MPa, well above the critical pressure of argon, which is approximately 5 MPa [48].

This approach failed for the smallest bubbles (<20 Å diameter), giving either negative or unphysically high pressures. The Van der Waals equation is known to break down in extreme cases and if the smallest gas bubbles are high-density fluids, then a gas equation of state would not be an appropriate way to describe them. Nevertheless, the more likely explanation in these cases is that two bubbles were overlapped in the beam path through the specimen, apparently giving a number of atoms per bubble about double the expected level, which would automatically give unphysical density and pressure results. Recent work on xenon and krypton bubbles formed by ion implantation showed that the Van der Waals equation did not give a wholly accurate description of the pressures within the bubbles, and tended to overestimate them [49].

The diameter and number of atoms were counted for 41 bubbles in total, the pressures calculated for 35 (since 6 had to be excluded for unphysically high densities, as accounted for above). The pressure inside the bubbles seems to decrease with bubble diameter but the large standard deviation makes it difficult to assess the exact nature of the relationship between diameter and pressure.

It is clear from both this and previous work that argon implants in these and other similar materials and forms bubbles on annealing. Having then established that high pressure argon bubbles do form on annealing, it is necessary to account for how these bubbles occur. The presence of the argon is easy to explain; the argon atoms become trapped in the coating during the relatively fast deposition process that is used to build the layers, which are hundreds of nanometres thick and used in both single-layer test samples and mulitlayer mirror coatings. The more pressing question is; why do the bubbles form? The process is not the same as that of noble gases deposited in materials by ion implantation, where each implanted atom has to displace others, causing highly strained positions in the lattice and where this strain can be reduced by the aggregation of the noble gas atoms. That is the case for xenon and krypton in nuclear reactor materials. Here, however, each argon atom does not bond with the atom around it but it will disrupt the bonding of the surrounding Ta_2O_5 glass. Therefore, it will still be in a high energy state that could be reduced by the argon atoms congregating in a similar manner to the previous example. This will only occur if there is enough thermal energy for the argon atoms to diffuse randomly, until they come close enough to each other; they will then group together and eventually form bubbles. The characteristic bubble size will then vary with annealing temperature, as is the case with any thermally activated process. If it were possible in future work to get statistically significant measures of mean bubble diameter after annealing at multiple temperatures, then it may be possible to estimate the average energy barrier to diffusion for an argon atom in the Ta_2O_5 glass. From this the average diffusion distance for a given annealing time and temperature could be estimated, as well as what proportion of the total argon will form visible nanobubbles. Molecular dynamics simulations could also shed light on this process if a suitably large cell

Optical Materials EXPRESS

could be constructed, with a reasonable number of argon atoms interspersed with the tantalum, oxygen and titanium atoms. This is, however, all work for further studies.

The optical properties of the films will almost certainly be affected by the bubbles. The first evidence of bubbles in these films (although at that point they were believed to be hollow voids) came from ellipsometry studies [11]. The characterisation presented in this paper is consistent with the conclusions of that study. Studies of mechanical loss – which is linked to thermal noise via the fluctuation-dissipation theorem [50] – note that mechanical loss initially decreases significantly with increased annealing temperature [51]. At higher annealing temperatures, however, the benefits from annealing no longer increase at the same rate [12]. The initial decrease may be because of structural relaxation from an initial 'frozen' state that is far from equilibrium. As for the smaller loss improvements at higher annealing temperatures, it may be that above a certain temperature the bubbles become a critical size, and where previously they were small enough to have little or no effect on the loss, they might now be large enough to appreciably affect the loss [13]. If this is the case, it would be a good candidate for an atomic modelling project to identify the mechanism causing the increased loss due to the larger bubbles. The larger size would also cause increased scattering loss in a gravitational wave detector [9], as the larger bubbles sizes also make it more likely that photons will be scattered or absorbed by the bubbles, rather than by the tantala-titania glass. There are several experiments that could be done to test this theory. The most obvious are X-ray scattering [12] and ellipsometry [11] experiments done in tandem with microscopy work to determine the size and distribution of the bubbles, on both as-deposited samples and samples annealed at a range of temperatures. Atomic modelling based on this experimental data would also be necessary in order to probe the mechanisms for increased loss due to bubble formation.

The technique detailed in this paper could be applied to other gas bubbles in other materials. It may be of particular interest in the nuclear field where bubbles of noble gases often form in nuclear reactor walls as the mechanics are very similar to gas bubbles formed during annealing of films made using ion-beam deposition.

4. Conclusion

Scanning transmission electron microscopy has been used to study the behaviour of argon in argon ion-beam assisted deposited thin films of Ta_2O_5 – TiO_2 mixed oxides of the type used for multilayer mirrors in the Advanced LIGO gravitational wave detectors (and similar detectors elsewhere in the world such as advanced Virgo). It is shown using HAADF imaging that bubbles start to form after annealing at 400 °C and coarsen after annealing at 600 °C to a mean diameter of 22 Å. It was found that argon could be unambiguously detected in the films using EELS, and that this was concentrated in the bubbles in the sample annealed at 600 °C. Using an argon $L_{2,3}$ edge from an older study together with a Hartree-Slater calculation for the cross-section well after the edge onset, a semi-empirical differential EELS cross-section was created and used for absolute quantification. This was then used to quantify the contents of 35 bubbles. It was found that these bubbles had a range of densities and pressures, with a mean density of 870 kg/m^3 and a mean pressure of 400 MPa. There was a weak trend towards lower pressure with increasing bubble diameter. It is currently unclear what influence the formation and coarsening of the bubbles has on the properties of the films, and whether changing the deposition process to remove the argon bubbles would be beneficial, although this should certainly be investigated in future work. Moreover, now it is clear that argon bubbles are present in most of these films, investigations including theoretical simulation-based studies should be conducted to understand their behaviour and whether they affect the optical or mechanical loss. Finally, the methodology used here for studying small noble gas bubbles is directly applicable to other noble gases in a range of materials, such as in cases of ion implantation.

Funding. Engineering and Physical Sciences Research Council (EP/R513222/1); Science and Technology Facilities

Optical Materials EXPRESS

Council (ST/I001085/1, ST/N005422/1).

Acknowledgements. This paper has LIGO DCC number P2000354.The data that support the findings of this study can be found in Enlighten: Research Data at 10.5525/gla.researchdata.1074.

The authors thank the Optics Working Group of the LIGO Scientific Collaboration (LSC) and the participants at the 2016 Gravitational Wave Advanced Detector Workshop (GWADW) for fruitful discussions that first raised the importance of argon within optical coatings. The authors would also like to thank Martin Hart for making the samples and for Hafizah Noor Isa for her work on characterising the composition of the matrix of the samples. For helpful discussions, the authors would also like to thank Prof. Alan J. Craven, Prof. Stuart Reid, Prof. Carmen Menoni, and Dr. Riccardo DeSalvo.

Disclosures. The authors declare no conflicts of interest.

Supplemental document. See Supplement 1 for supporting content.

References

1. B. P. Abbott, "Observation of gravitational waves from a binary black hole merger," Phys. Rev. Lett. **116**(6), 061102 (2016).
2. LIGO Scientific Collaboration and Virgo Collaboration, "Gw151226: Observation of gravitational waves from a 22-solar-mass binary black hole coalescence," Phys. Rev. Lett. **116**(24), 241103 (2016).
3. LIGO Scientific Collaboration and Virgo Collaboration, "GW170814: A three-detector observation of gravitational waves from a binary black hole coalescence," Phys. Rev. Lett. **119**(14), 141101 (2017).
4. The LIGO Scientific Collaboration and The Virgo Collaboration, "GW170817: Observation of gravitational waves from a binary neutron star inspiral," Phys. Rev. Lett. **119**(16), 161101 (2017).
5. B. P. Abbott, R. Abbott, T. D. Abbott, M. R. Abernathy, F. Acernese, K. Ackley, C. Adams, T. Adams, P. Addesso, and R. X. Adhikari, *et al.*, "GWTC-1: A gravitational-wave transient catalog of compact binary mergers observed by LIGO and Virgo during the first and second observing runs," arXiv:1811.12907 (2018).
6. B. P. Abbott, R. Abbott, T. D. Abbott, F. Acernese, K. Ackley, C. Adams, T. Adams, P. Addesso, R. X. Adhikari, and V. B. Adya, "GW170104: Observation of a 50-solar-mass binary black hole coalescence at redshift 0.2," Phys. Rev. Lett. **118**(22), 221101 (2017).
7. LIGO Scientific Collaboration and Virgo Collaboration, "GW150914: The advanced LIGO detectors in the era of first discoveries," *Phys. Rev. Lett.* 116(13), 131103 (2016).
8. F. Acernese et al., "Advanced Virgo: a second-generation interferometric gravitational wave detector," Classical Quantum Gravity **32**(2), 024001 (2014).
9. M. Granata, E. Saracco, N. Morgado, A. Cajgfinger, G. Cagnoli, J. Degallaix, V. Dolique, D. F. J. Franc, C. Michel, L. Pinard, and R. Flaminio, "Mechanical loss in state-of-the-art amorphous optical coatings," Phys. Rev. D **93**(1), 012007 (2016).
10. G. M. Harry, M. R. Abernathy, A. E. Becerra-Toledo, H. Armandula, E. Black, K. Dooley, M. Eichenfield, C. Nwabugwu, A. Villar, D. R. M. Crooks, G. Cagnoli, J. Hough, C. R. How, I. MacLaren, P. Murray, S. Reid, S. Rowan, P. H. Sneddon, M. M. Fejer, R. Route, S. D. Penn, P. Ganau, J.-M. Mackowski, C. Michel, L. Pinard, and A. Remillieux, "Titania-doped tantala/silica coatings for gravitational-wave detection," Classical Quantum Gravity **24**(2), 405–415 (2006).
11. L. Anghinolfi, M. Prato, A. Chtanov, M. Gross, A. Chincarini, M. Neri, G. Gemme, and M. Canepa, "Optical properties of uniform, porous, amorphous Ta2O5 coatings on silica: temperature effects," J. Phys. D: Appl. Phys. **46**(45), 455301 (2013).
12. K. Prasai, J. Jiang, A. Mishkin, B. Shyam, S. Angelova, R. Birney, D. A. Drabold, M. Fazio, E. K. Gustafson, G. Harry, S. Hoback, J. Hough, C. L'evesque, I. MacLaren, A. Markosyan, I. W. Martin, C. S. Menoni, P. G. Murray, S. Penn, S. Reid, R. Robie, S. Rowan, F. Schiettekatte, R. Shink, A. Turner, G. Vajente, H.-P. Cheng, M. M. Fejer, A. Mehta, and R. Bassiri, "High precision detection of change in intermediate range order of amorphous zirconia-doped tantala thin films due to annealing," Phys. Rev. Lett. **123**(4), 045501 (2019).
13. C. Harthcock, S. Qiu, R. Negres, J. Hammons, T. Voisin, G. Guss, A. Martin, C. Stolz, M. Menor, G. Bhowmik, and M. Huang, "The impact of nano-bubbles on the laser performance of hafnia films deposited by oxygen assisted ion beam sputtering method," Appl. Phys. Lett. **115**(25), 251902 (2019).
14. M. A. Fazio, G. Vajente, A. Ananyeva, A. Markosyan, R. Bassiri, M. M. Fejer, and C. S. Menoni, "Structure and morphology of low mechanical loss tio2-doped ta2o5," Opt. Mater. Express **10**(7), 1687–1703 (2020).
15. R. Barnes and D. Mazey, "The nature of radiation-induced point defect clusters," Philos. Mag. **5**(60), 1247–1253 (1960).
16. R. Barnes and D. Mazey, "The migration and coalescence of inert gas bubbles in metals," Proc. R. Soc. Lond. A **275**(1360), 47–57 (1963).
17. G. Greenwood, A. Foreman, and D. Rimmer, "The role of vacancies and dislocations in the nucleation and growth of gas bubbles in irradiated fissile material," J. Nucl. Mater. **1**(4), 305–324 (1959).
18. S. Pennycook and D. Jesson, "High-resolution Z-contrast imaging of crystals," Ultramicroscopy **37**(1-4), 14–38 (1991).
19. K. Nogita and K. Une, "High resolution TEM observation and density estimation of Xe bubbles in high burnup UO2 fuels," Nucl. Instrum. Methods Phys. Res., Sect. B **141**(1-4), 481–486 (1998).

Optical Materials EXPRESS

20. M. Klimiankou, R. Lindau, and A. Möslang, "Energy-filtered TEM imaging and EELS study of ODS particles and argon-filled cavities in ferritic–martensitic steels," Micron **36**(1), 1–8 (2005).
21. M. Watanabe and D. Williams, "The quantitative analysis of thin specimens: a review of progress from the Cliff-Lorimer to the new zeta-factor methods," J. Microsc. **221**(2), 89–109 (2006).
22. K. MacArthur, T. Slater, S. Haigh, D. Ozkaya, P. Nellist, and S. Lozano-Perez, "Quantitative energy-dispersive X-ray analysis of catalyst nanoparticles using a partial cross-section approach," Microsc. Microanal. **22**(1), 71–81 (2016).
23. A. J. Craven, J. Bobynko, B. Sala, and I. MacLaren, "Accurate measurement of absolute experimental inelastic mean free paths and EELS differential cross-sections," Ultramicroscopy **170**, 113–127 (2016).
24. A. J. Craven, B. Sala, J. Bobynko, and I. MacLaren, "Spectrum imaging of complex nanostructures using DualEELS: II. Absolute quantification using standards," Ultramicroscopy **186**, 66–81 (2018).
25. M. Blackmur, S. Dumbill, I. MacLaren, D. Hernandez-Maldonado, P. Styman, M. Gass, R. Nicholls, J. Hyde, Q. Ramasse, K. Annand, J. Smith, and N. Gotham, "The association of hydrogen with nanometre bubbles of helium implanted into zirconium," Scr. Mater. **152**, 102–106 (2018).
26. K. Izui, K. Hojou, S. Furuno, K. Ono, and T. Kino, "Electron energy loss spectroscopy of helium injected in aluminum at high temperature," J. Electron Microsc. **33**, 381–383 (1984).
27. F. Vasiliu, I. Teodorescu, and F. Glodeanu, "SEM investigations of iron surface ion erosion as a function of specimen temperature and incidence angle," J. Mater. Sci. **10**(3), 399–405 (1975).
28. A. Gubbens, M. Barfels, C. Trevor, R. Twesten, P. Mooney, P. Thomas, N. Menon, B. Kraus, C. Mao, and B. McGinn, "The GIF quantum, a next generation post-column imaging energy filter," Ultramicroscopy **110**(8), 962–970 (2010).
29. J. Scott, P. Thomas, M. MacKenzie, S. McFadzean, J. Wilbrink, A. Craven, and W. Nicholson, "Near-simultaneous dual energy range EELS spectrum imaging," Ultramicroscopy **108**(12), 1586–1594 (2008).
30. C. Ahn and O. Krivanek, *EELS Atlas: A Reference Guide of Electron Energy Loss Spectra Covering All Stable Elements* (Gatan, 1983).
31. R. Egerton, "Oscillator-strength parameterization of inner-shell cross-sections," Ultramicroscopy **50**(1), 13–28 (1993).
32. H. N. Isa, "Towards reliable quantification of mixed oxide coating for LIGO using DualEELS," Ph.D. thesis, University of Glasgow (2019).
33. M. J. Hart, R. Bassiri, K. B. Borisenko, M. Veron, E. F. Rauch, I. W. Martin, S. Rowan, M. M. Fejer, and I. MacLaren, "Medium range structural order in amorphous tantala spatially resolved with changes to atomic structure by thermal annealing," J. Non-Cryst. Solids **438**, 10–17 (2016).
34. J. Bobynko, I. MacLaren, and A. J. Craven, "Spectrum imaging of complex nanostructures using DualEELS: I. digital extraction replicas," Ultramicroscopy **149**, 9–20 (2015).
35. G. Lucas, P. Burdet, M. Cantoni, and C. Hebert, "Multivariate statistical analysis as a tool for the segmentation of 3D spectral data," Micron **52-53**, 49–56 (2013).
36. R. F. Egerton, *Electron Energy-loss Spectroscopy in the Electron Microscope* (Springer, 2011), 3rd ed.
37. R. Webster, A. Craven, B. Schaffer, S. McFadzean, I. MacLaren, and D. MacLaren, "Correction of eels dispersion non-uniformities for improved chemical shift analysis," Ultramicroscopy **217**, 113069 (2020).
38. K. J. Annand, I. MacLaren, and M. Gass, "Utilising DualEELS to probe the nanoscale mechanisms of the corrosion of zircaloy-4 in 350 $^{\circ}$C pressurised water," J. Nucl. Mater. **465**, 390–399 (2015).
39. J. D. van der Waals, "Over de Continuiteit van den Gas - en Vloeistoftoestand," Ph.D. thesis, University of Leiden (1873). (On the continuity of the gaseous and liquid state).
40. R. C. Weast, *CRC Handbook of Chemistry and Physics* (CRC Press, 1972), 53rd ed.
41. J. D. Hunter, "Matplotlib: A 2D graphics environment," Comput. Sci. Eng. **9**(3), 90–95 (2007).
42. D. Potter and C. Rossouw, "High resolution of crystalline xenon and xenon alloys in aluminium," J. Nucl. Mater. **161**(2), 124–131 (1989).
43. J. H. Evans and D. J. Mazey, "Evidence for solid krypton bubbles in copper, nickel and gold at 293k," J. Phys. F: Met. Phys. **15**(1), L1–L6 (1985).
44. A. vom Felde, J. Fink, T. Muller-Heinzerling, J. Pfluger, B. Scheerer, G. Linker, and D. Kaletta, "Pressure of neon, argon, and xenon bubbles in aluminum," Phys. Rev. Lett. **53**(9), 922–925 (1984).
45. S. Donnelly and C. Rossouw, "Lattice images of inert gas bubbles in aluminium," Nucl. Instrum. Methods Phys. Res., Sect. B **13**(1-3), 485–489 (1986).
46. C. J. Rossouw and S. E. Donnelly, "Superheating of small solid-argon bubbles in aluminum," Phys. Rev. Lett. **55**(27), 2960–2963 (1985).
47. K. Iakoubovskii, K. Mitsuishi, Y. Nakayama, and K. Furuya, "Mean free path of inelastic electron scattering in elemental solids and oxides using transmission electron microscopy: Atomic number dependent oscillatory behavior," Phys. Rev. B **77**(10), 104102 (2008).
48. W. McCain and T. Ziegler, "Critical temperature, critical pressure, and vapor pressure of argon," J. Chem. Eng. Data **12**(2), 199–202 (1967).
49. A. Jelea, "An equation of state for xenon/krypton mixtures confined in the nuclear fuels," J. Nucl. Mater. **530**, 151952 (2020).
50. H. H. B. Callen and R. Greene, "On a theorem of irreversible thermodynamics," Phys. Rev. **86**(5), 702–710 (1952).
51. G. Vajente, R. Birney, A. Ananyeva, S. Angelova, R. Asselin, B. Baloukas, R. Bassiri, G. Billingsley, M. M. Fejer, D. Gibson, L. J. Godbout, E. Gustafson, A. Heptonstall, J. Hough, S. MacFoy, A. Markosyan, I. W. Martin, L. Martinu, P.

Optical Materials EXPRESS

G. Murray, S. Penn, S. Roorda, S. Rowan, F. Schiettekatte, R. Shink, C. Torrie, D. Vine, S. Reid, and R. X. Adhikari, "Effect of elevated substrate temperature deposition on the mechanical losses in tantala thin film coatings," Classical Quantum Gravity **35**(7), 075001 (2018).